



## RESEARCH ARTICLE

10.1002/2016RS005957

## Key Points:

- Simultaneous observations of the OCB using optics and radar
- SWB-AEB offset more related to the solar cycle and MLT variations
- High-density EUV ionized plasma cause beam refraction

## Correspondence to:

X.-C. Chen,  
xiangcai.chen@unis.no

## Citation:

Chen, X.-C., D. A. Lorentzen, J. I. Moen, K. Oksavik, L. J. Baddeley, and M. Lester (2016), *F* region ionosphere effects on the mapping accuracy of SuperDARN HF radar echoes, *Radio Sci.*, 51, 490–506, doi:10.1002/2016RS005957.

Received 25 JAN 2016

Accepted 28 APR 2016

Accepted article online 3 MAY 2016

Published online 19 MAY 2016

## *F* region ionosphere effects on the mapping accuracy of SuperDARN HF radar echoes

X.-C. Chen<sup>1,2,3</sup>, D. A. Lorentzen<sup>1,2,4</sup>, J. I. Moen<sup>1,3</sup>, K. Oksavik<sup>1,2</sup>, L. J. Baddeley<sup>1,2,4</sup>, and M. Lester<sup>5</sup>

<sup>1</sup>Department of Arctic Geophysics, University Centre in Svalbard, Longyearbyen, Norway, <sup>2</sup>Birkeland Centre for Space Science, Department of Physics and Technology, University of Bergen, Bergen, Norway, <sup>3</sup>Department of Physics, University of Oslo, Oslo, Norway, <sup>4</sup>British Antarctic Survey, Cambridge, UK, <sup>5</sup>Department of Physics and Astronomy, University of Leicester, Leicester, UK

**Abstract** Structured particle precipitation in the cusp is an important source for the generation of *F* region ionospheric irregularities. The equatorward boundaries of broad Doppler spectral width in Super Dual Auroral Radar Network (SuperDARN) data and the concurrent OI 630.0 nm auroral emission are good empirical proxies for the dayside open-closed field line boundary. However, SuperDARN currently employs a simple virtual model to determine the location of its echoes, instead of a direct calculation of the radio wave path. The varying ionospheric conditions could influence the final mapping accuracy of SuperDARN echoes. A statistical comparison of the offsets between the SuperDARN Finland radar spectral width boundary (SWB) and the OI 630.0 nm auroral emission boundary (AEB) from a meridian-scanning photometer (MSP) on Svalbard is performed in this paper. By restricting the location of the 630.0 nm data to be near local zenith where the MSP has the highest spatial resolution, the optical mapping errors were significantly reduced. The variation of the SWB-AEB offset confirms that there is a close relationship between the mapping accuracy of the HF radar echoes and solar activity. The asymmetric variation of the SWB-AEB offset versus magnetic local time suggests that the intake of high-density solar extreme ultraviolet ionized plasma from postnoon at subauroral latitudes could result in a stronger refraction of the HF radar signals in the noon sector, while changing the HF radar operating frequency also has a refraction effect that contributes to the final location of the HF radar echoes.

### 1. Introduction

The Super Dual Auroral Radar Network (SuperDARN) has been a very successful tool for monitoring dynamical processes in the polar ionosphere [e.g., Greenwald *et al.*, 1985, 1995; Chisham *et al.*, 2007]. For SuperDARN, being an over-the-horizon radar system, the background ionospheric electron density is a crucial factor for the propagation of the HF radio waves [e.g., Milan *et al.*, 1997; Danskin *et al.*, 2002; Koustov *et al.*, 2014]. By using transmitter frequencies between 8 and 20 MHz, SuperDARN is sensitive to field-aligned plasma density irregularities on the Bragg scale [Greenwald *et al.*, 1985; Chisham *et al.*, 2007]. The maximum backscatter power is returned when the refracted radio wave vector is nearly orthogonal to the local Earth's magnetic field [Greenwald *et al.*, 1995]. The ionospheric backscatter therefore depends on both the occurrence of the field-aligned plasma density irregularities [e.g., Baker *et al.*, 1986; Moen *et al.*, 2002] and gradients in the ionospheric electron density [e.g., Ponomarenko *et al.*, 2009].

SuperDARN typically uses a seven-pulse transmitter sequence to determine the complex autocorrelation function (ACF) of the echoes [Greenwald *et al.*, 1985]. The derivative of the ACF phase with respect to time lag is used to estimate the Doppler line-of-sight velocity [e.g., Greenwald *et al.*, 2008], while the decay time of the ACF power gives the Doppler spectral width [e.g., Baker *et al.*, 1995; Ponomarenko and Waters, 2006]. For more than two decades, these data products have been widely used by the international scientific community. Applications, for instance, include the determination of global maps of ionospheric convection [e.g., Cousins and Shepherd, 2010] and studies of the variation of the polar cap area during substorm cycles [e.g., Milan *et al.*, 2003b].

An area of significant emphasis in the literature is the equatorward boundary of OI 630.0 nm cusp auroral forms, which is believed to be the ionospheric footprint of the open-closed field line boundary (OCB) [Lorentzen *et al.*, 1996; Milan *et al.*, 1999; Moen *et al.*, 1996, 1998, 2001; Oksavik *et al.*, 2000, 2004a]. On the poleward side of the ionospheric OCB the cusp plasma becomes hot [Moen *et al.*, 2004], which is indicative of

enhanced magnetopause reconnection [Lockwood *et al.*, 1989]. In principle, this boundary should be easy to detect also from SuperDARN data, and many investigations have looked at the collocation of the HF radar cusp and the cusp aurora [e.g., Rodger *et al.*, 1995; Milan *et al.*, 1999; Moen *et al.*, 2001, 2002; Oksavik *et al.*, 2004b]. These studies have compared the location of the transition from narrow to broad HF radar spectral width with the concurrent OI 630.0 nm auroral emission boundary (AEB). Surprisingly, often, there is an offset in latitude.

Rodger *et al.* [1995] observed HF radar echo boundaries that on average were  $0.5^\circ$  equatorward of the optical AEB, which agrees with Oksavik *et al.* [2004b]. Conversely, Milan *et al.* [1999] and Moen *et al.* [2001] found the optical AEB was located slightly equatorward of the HF radar cusp. Moen *et al.* [2001] also tried to compensate by assuming different auroral emission altitudes. Oksavik *et al.* [2011] used a ground range offset of 140 km to align the HF radar echo with optical signatures associated with a reversed flow event. Statistically, Chisham *et al.* [2005a, 2005c] and Sotirelis *et al.* [2005] confirmed that a close relationship between the spectral width boundary (SWB) and the ionospheric open-closed field line boundary (OCB) from the Defense Meteorological Satellite Program (DMSP) particle precipitation data. Chisham *et al.* [2005a, 2005c] showed that the HF radar SWB was  $\sim 1^\circ$  latitude poleward of the DMSP particle precipitation boundary (PPB). Sotirelis *et al.* [2005] observed that the offset varies from zero near noon to  $\sim 1^\circ$  near dawn and dusk. Yeoman *et al.* [2001] used the European Incoherent Scatter Heating facility to produce artificial irregularities, and they found a ground range error of 114 km for  $1\frac{1}{2}$ -hop SuperDARN echoes. Consequently, the subsequent similar experiments imply that the SuperDARN ground range error is often underestimated due to the varying ionospheric conditions [Yeoman *et al.*, 2008]. However, the interrelationship of the varying ionospheric densities that gives rise to the varied mapping errors is still not well understood [Chisham *et al.*, 2008].

It is well known that the high-latitude *F* region ionosphere is influenced by both magnetospheric convection and particle precipitation [e.g., Lockwood *et al.*, 1990; Cowley, 2000]. Two different categories of ionospheric plasma are thus comprised. Due to magnetospheric convection a low-density background plasma and a high-density solar extreme ultraviolet (EUV) ionized plasma that flows through the cusp inflow region and into the polar cap from subauroral latitudes [Knudsen, 1974; Foster, 1984; Sojka *et al.*, 1994]. During geomagnetic storms the high-density plasma can form a continuous tongue-of-ionization (TOI) that extends into the polar cap and greatly enhance the *F* region electron density [Foster *et al.*, 2004, 2005]. The TOI can be further restructured into polar cap patches when it crosses the dayside OCB [Carlson *et al.*, 2004, 2006; Moen *et al.*, 2006; Lorentzen *et al.*, 2010; Oksavik *et al.*, 2006, 2010; Zhang *et al.*, 2011, 2013a, 2015]. Nevertheless, soft electron precipitation (having energy less than several hundred eV [Newell and Meng, 1992]) only adds structured plasma in the cusp ionosphere, compared to subauroral latitudes [Zhang *et al.*, 2013b]. They will produce 10 m scale plasma irregularities at kilometer-scale electron density gradients in the *F* region, which was recently verified by Moen *et al.* [2012] and Oksavik *et al.* [2012] using high-resolution data from the ICI-2 sounding rocket.

The ground projection of SuperDARN echoes is currently determined by assuming a straight-line propagation of the radio wave to a fixed virtual height (400 km at far ranges). It does not account for the prevailing conditions in the ionosphere, which will give rise to varied mapping errors compared to the actual location of the ionospheric plasma irregularities [e.g., Yeoman *et al.*, 2001, 2008; Chisham *et al.*, 2008]. Ray tracing based on model electron densities could in principle improve the ground projection of HF radar echoes [Villain *et al.*, 1984; Liu *et al.*, 2012], but accurate determination of the propagation path within the highly varying background ionosphere is difficult at far ranges [André *et al.*, 1997; Ponomarenko *et al.*, 2009]. Furthermore, model like the International Reference Ionosphere (IRI) only describes the ionospheric electron densities as monthly averages [Bilitza *et al.*, 2014], which does not account for the time-varying conditions in the ionosphere.

The SuperDARN Finland radar overlaps the field of view of a meridian-scanning photometer (MSP) in Svalbard; an alternative method for measuring the mapping accuracy of HF radar echoes was recently introduced by Chen *et al.* [2015]. With high spatial resolution when the aurora is near local zenith, the mapping error due to the assumed auroral emission height becomes insignificant [Johnsen and Lorentzen, 2012a; Chen *et al.*, 2015]. It allows for the offset between the HF radar echoes and the auroral emissions to be quantified. By using simultaneous observations of ground-based optical and HF radar OCBs along the

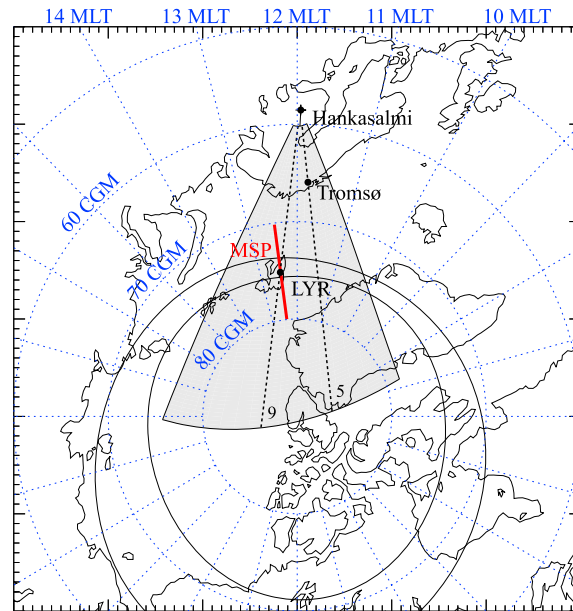


**Figure 1.** Field of view of the SuperDARN Finland radar (grey shading) and the MSP meridian (red line) in AACGM coordinates at 09:30 UT. Radar beams 5 and 9 intersect Tromsø and Longyearbyen, respectively. The statistical location of the auroral oval is also indicated for  $K_p = 1$ .

operating frequencies is analyzed and discussed in sections 3 and 4, respectively. Section 5 summarizes the importance of the varied  $F$  region plasma density contribution to the SWB-AEB offset.

## 2. Instrumentation and Data Processing

### 2.1. Spectral Width Data From the SuperDARN Finland Radar

The SuperDARN Finland radar is located at Hankasalmi (62.3°N, 26.6°E). It is part of CUTLASS (Co-operative UK Twin Located Auroral Sounding System), and it has been in operation since 1995. In its most common operating mode the radar has 16 beams. Each beam is approximately 3.2° wide in azimuth and starting from 12° west of geographic north, while a pulse length of 300 μs corresponds to a radar range gate length of 45 km [Milan et al., 1997]. The first gate is located at 180 km range, and for each beam a total of 75 range gates is usually recorded. The radar thus completes a full scan in either 60 or 120 s [Lester et al., 2004]. This work only utilizes common mode data, which have been preprocessed using the same version of the SuperDARN software (fitACF v.1.09, e.g., using the modifications to the ACF processing as described by Ponomarenko and Waters [2006]). Beam 9 intersects the Longyearbyen (LYR) MSP at the ~1890 km range (see Figure 1). From the received signal-to-noise ratios the ionospheric plasma Doppler line-of-sight velocity, the Doppler spectral power, and the Doppler spectral width can be derived [Greenwald et al., 1995].

### 2.2. Auroral Data From the Meridian-Scanning Photometer (MSP)

The MSP is located at LYR (78.2°N, 15.8°E) and provides the ground-based optical observation of auroral boundaries. The MSP has a rotating mirror that scans along the geomagnetic meridian. The time resolution is 16 s, and the emission intensity is measured in Rayleigh for scan angles ranging from 0° to 180° (from north to south) at an angular resolution of ~1°. The background emissions were subtracted from the peak emissions using tilting interference filters [Romick, 1976]. Five channels, which include red (OI 630.0 nm) and green (OI 557.7 nm) auroral emissions, are recorded simultaneously. In 2007 the old Aurora Station was relocated to the new Kjell Henriksen Observatory (Altitude Adjusted Corrected Geomagnetic (AACGM): 75.2°N, 111.1°E). Except for the 2005/2006 and 2006/2007 winter seasons, these optical data are available from 15 auroral seasons since 1994/1995.

geomagnetic meridian, Chen et al. [2015] suggested that transient dayside reconnection could segment the intake of solar EUV ionized plasma from subauroral latitudes, increasing the background ionospheric density, and give rise to an excessive mapping error. The mapping has particular importance for studies using HF radar data on small and mesoscale size. Improved mapping is required for accurate tracking of polar cap patches [e.g., Lorentzen et al., 2010; Oksavik et al., 2010; Zhang et al., 2013a; Nishimura et al., 2014] and for space weather forecasting [Moen et al., 2013].

The current paper investigates the long-term variation of the latitude offsets between the HF radar SWB and the OI 630.0 nm AEB in the high-latitude dayside ionosphere and its relationship to the varying background ionospheric condition. This statistical study gives an overview of the instrumentation and data processing in section 2. The relationship of the latitude offsets between the HF radar SWB and the concurrent OI 630.0 nm AEB with the solar activity, MLT and different HF radar

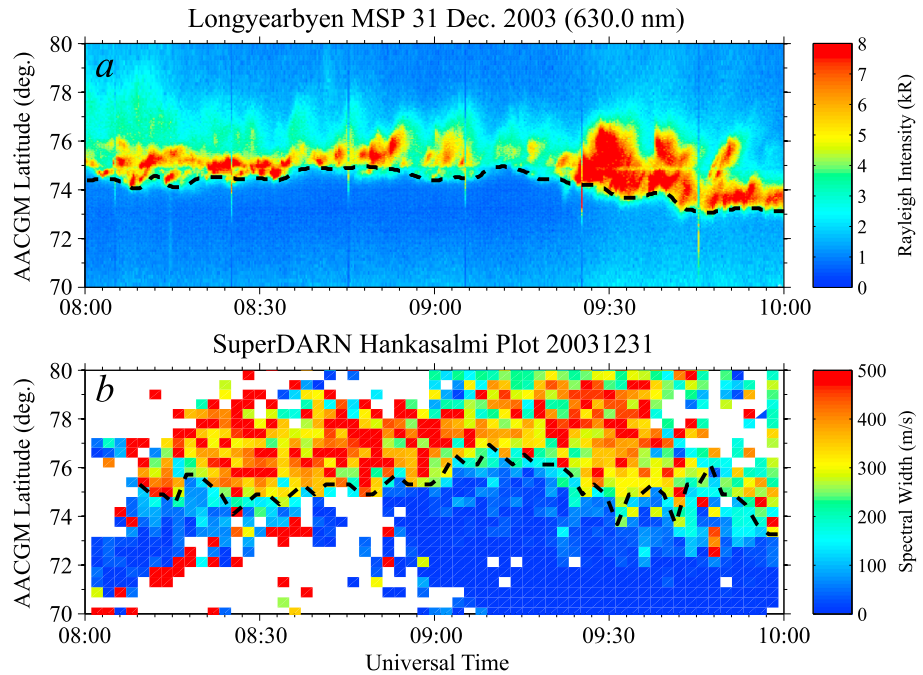


**Figure 2.** An example of the simultaneous (a) MSP keogram for the OI 630.0 nm auroral emission and (b) median-filtered ionospheric spectral width observations from the SuperDARN Finland radar. The vertical axes are AACGM latitude, and time runs along the horizontal axis. The black dashed curve in each panel represents the identified AEB and SWB, respectively.

### 2.3. Boundary Identifications

The equatorward boundaries of the OI 630.0 nm auroral emission and the latitude transition from narrow to broad spectral width must be simultaneously identified. For each MSP meridian scan, a search is performed to identify where the gradient of the emission intensity maximizes in order to trace the OI 630.0 nm AEB. The mapping height as a function of MSP scan angle, with a set of equations describing the mapping error, is used in this study (see *Johnsen et al.* [2012] for more details). The validity of this method has been confirmed by a number of case studies [*Johnsen and Lorentzen*, 2012a] and by statistical comparison [*Johnsen and Lorentzen*, 2012b]. To avoid the large mapping errors associated with MSP scan angles close to the horizon, only the boundaries from MSP scan angles between 40° and 150° were used (i.e., corresponding to the region directly overhead of the observation site, magnetic zenith at 98°). By means of trigonometry, the geographic latitude and longitude are calculated based on the assumed height for the emission (i.e., 303, 268, and 264 km at scan angles 40°, zenith, and 150°, respectively). The Altitude Adjusted Corrected Geomagnetic (AACGM) [*Baker and Wing*, 1989] latitude is used to project the OI 630.0 nm AEB and HF radar SWB into the same coordinate system.

An improved method for automatically identifying the HF radar SWB along the MSP meridian has been presented by *Chen et al.* [2015]. This method is similar to the *Chisham and Freeman* [2003] “C-F threshold technique,” i.e., using a spectral width threshold value that normally originates from typical cusp backscatter and searching poleward along the radar range gate until this threshold is exceeded. However, more criteria (see *Chen et al.* [2015] for more details) are implemented to eliminate any false boundary identifications due to lack of echoes; hence, the problem with unreliable boundaries for beams away from the meridional direction [*Chisham et al.*, 2005b] can be avoided. A high time resolution (2 min) estimate of the HF radar SWB is finally obtained [*Chen et al.*, 2015].

In spite of the fact that the interpretation of the broad spectral width remains elusive, the spectral width typically shows broad values around the cusp [e.g., *Baker et al.*, 1995]. The SWB represents a transition from low to high spectral width values with increased geomagnetic latitude (MLAT) [e.g., *Moen et al.*, 2001; *Chisham and Freeman*, 2004; *Freeman and Chisham*, 2004]. Due to the fact that ionospheric irregularity lifetime is essentially independent of the scale size [e.g., *Vallières et al.*, 2003; *Ponomarenko et al.*, 2007], the broad spectral width values will decrease with increasing HF radar operating frequency. *Ponomarenko et al.* [2007] found that

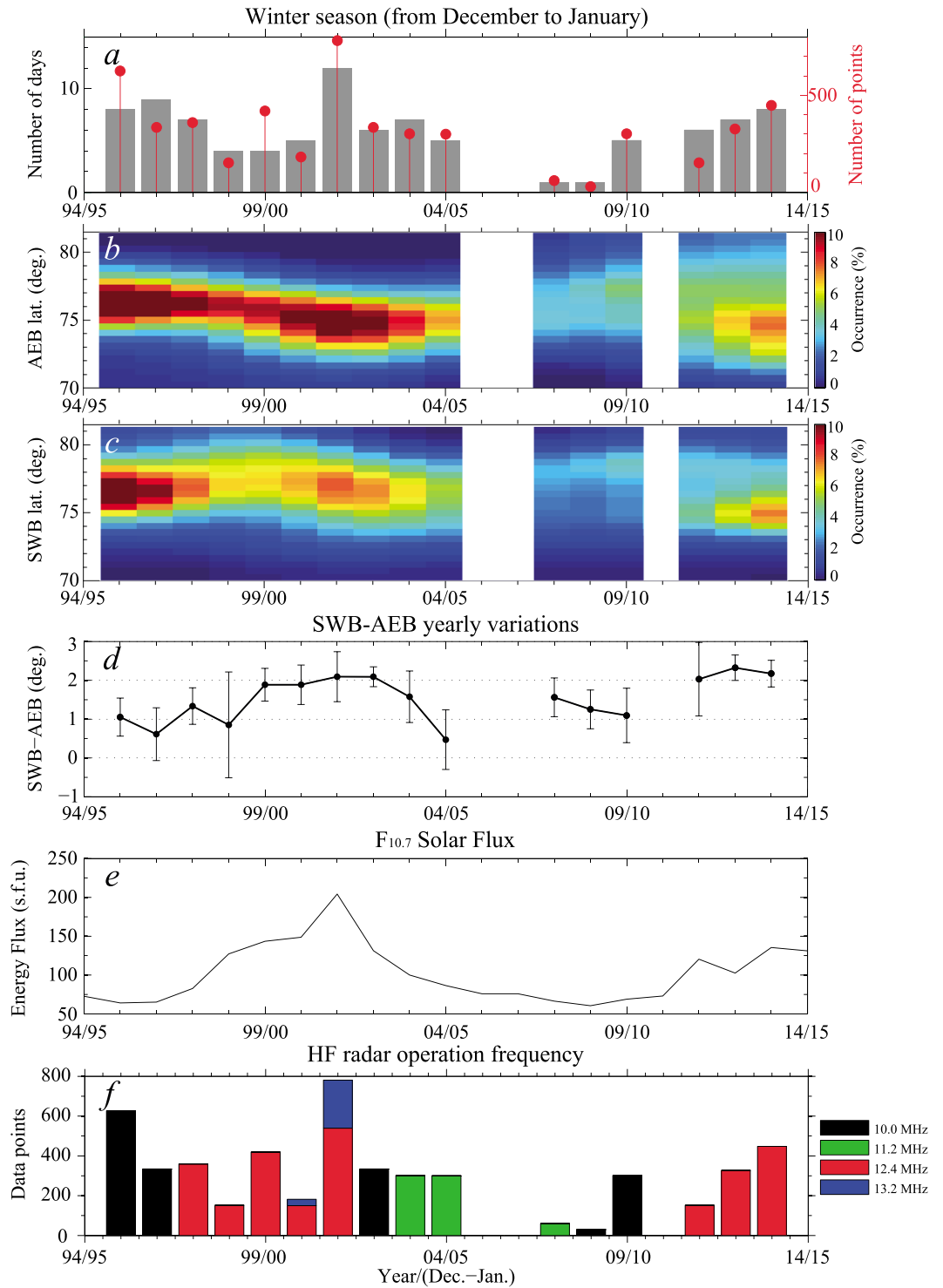


**Figure 3.** (a) The number of days (grey bars) and individual data points (red item) for each winter season. The latitudinal normalized occurrences of (b) AEB and (c) SWB from the MSP and HF radar observations, respectively. (d) The variation (with standard deviation represents error bars) of SWB-AEB offset in latitude along the magnetic meridian. (e) The monthly averaged  $F_{10.7}$  solar flux. (f) The distribution of data points by different HF radar operating frequencies.

the “normalized” spectral width,  $F = 1/\tau_{\text{corr}} \approx 2\pi \cdot f_0 \cdot W/c$ , is more suitable for representing the spectral width  $W$ , which is determined by the irregularity lifetime ( $\tau_{\text{corr}}$ ) mechanisms [Ponomarenko and Waters, 2006]. The  $f_0$  is the radar frequency, and  $c$  is the speed of light, and taking 40 Hz as the typical normalized spectral width [Ponomarenko et al., 2007], the selected spectral width threshold values linearly varied between 150 and 200 m/s with the HF radar operating frequency in the current study.

The time interval chosen for this study was 12:00 ± 3 MLT (magnetic noon at LYR is ~09:00 UT). By manual removal of days with bad, missing, or otherwise unusable optical data, and days without ionospheric backscatter, a total of 92 events (of different duration) of simultaneous good optical and HF radar observations was chosen for the statistical analysis. The optical and radar data were reduced to 2 min time resolution in order to ease the comparison. Figure 2 shows an example of the simultaneous boundary determinations of AEB and SWB (black dashed curves) from the two instruments.

### 3. Results

#### 3.1. Yearly Variability

The number of usable days for each winter season is shown by bar plots in Figure 3a. Each vertical red stem represents the corresponding number of comparable data points, with 2 min time resolution between HF radar SWB and OI 630.0 nm AEB. The horizontal time axis represents the winter auroral seasons from December to January. Due to instrument malfunction, the data for winter seasons 2005/2006 and 2006/2007 are unavailable (see section 2.2). The missing data for the 2010/2011 season is due to bad weather and few HF radar echoes.

The normalized yearly occurrences of the OI 630.0 nm AEB and HF radar SWB with 0.5° latitude resolution are shown in Figures 3b and 3c, respectively. Figure 3b indicates that the OI 630.0 nm AEB is located slightly north of geomagnetic zenith (AEB: 75.62° MLAT on average), which is consistent with previous cusp particle precipitation data from the DMSP satellites [e.g., Newell and Meng, 1992]. The envelope of the OI 630.0 nm AEB distribution shifts to lower latitude for winter seasons 2002/2003, 2011/2012, and 2013/2014, which is approximately associated with the enhanced  $F_{10.7}$  solar radio flux seen in Figure 3e. This implies that the solar wind driving during these years was significantly higher than the remaining interval, thus expanding the polar cap due to the increased energy input [Milan et al., 2012]. The HF radar SWB in Figure 3c displays a latitude distribution with the majority of SWBs around 77.29° MLAT, which is ~1.5° (i.e., ~160 km), on average, farther poleward than the AEB.

The yearly variation of the median-filtered SWB-AEB offset, with error bars representing the standard deviation, is shown in Figure 3d. While Figure 3f shows the distribution of comparable data points for different radar operating frequencies. Four frequencies (around 10.0, 11.2, 12.4 and 13.2 MHz) were mainly used during the winter season. When the  $F_{10.7}$  solar flux increases, it can be seen that the SWB-AEB offset also shows a slight increase (with the one exception being the winter season 1998/1999). To investigate the dependence on solar cycle, the winter seasons 1999/2000–2003/2004 (cycle 23) and 2011/2012–2013/2014 (cycle 24) will be used as a proxy for solar maxima [e.g., Bjoland et al., 2015], while the rest of the season for solar minima (i.e., 1995/1996–1998/1999 and 2004/2005–2009/2010). Using this definition, the averaged SWB for solar maxima (minima) is found to be ~2° (~1°), on average, poleward of the AEB.

#### 3.2. Diurnal Variability

The number of data points as a function of MLT, with the same colors as Figure 3f representing different HF radar operating frequencies, is shown in Figures 4a and 4b for solar maxima and minima, respectively. Only three frequencies were used at solar minima. The distributions illustrate that most HF radar echoes occurred at ~11:00–14:00 MLT. An asymmetric distribution of the data points at 12.4 (10.0) MHz radar frequency, indicates that the occurrence of the HF radar echoes tends to be in the prenoon (postnoon) sector for solar maxima (minima).

To ensure reliable results, only intervals having more than 150 data points (red bars >150 in Figure 4a, and black bars >150 in Figure 4b) were used for more specific comparison. The red line in Figure 4c shows the mean AEB latitudes versus MLT for solar maxima and 12.4 MHz radar frequency. The AEB is on average situated at ~75.48° MLAT, and slightly lower in the prenoon sector (~09:00–11:00 MLT) than in the noon and postnoon sectors (~11:00–15:00 MLT). The distribution of mean SWB (grey line) also shows a similar

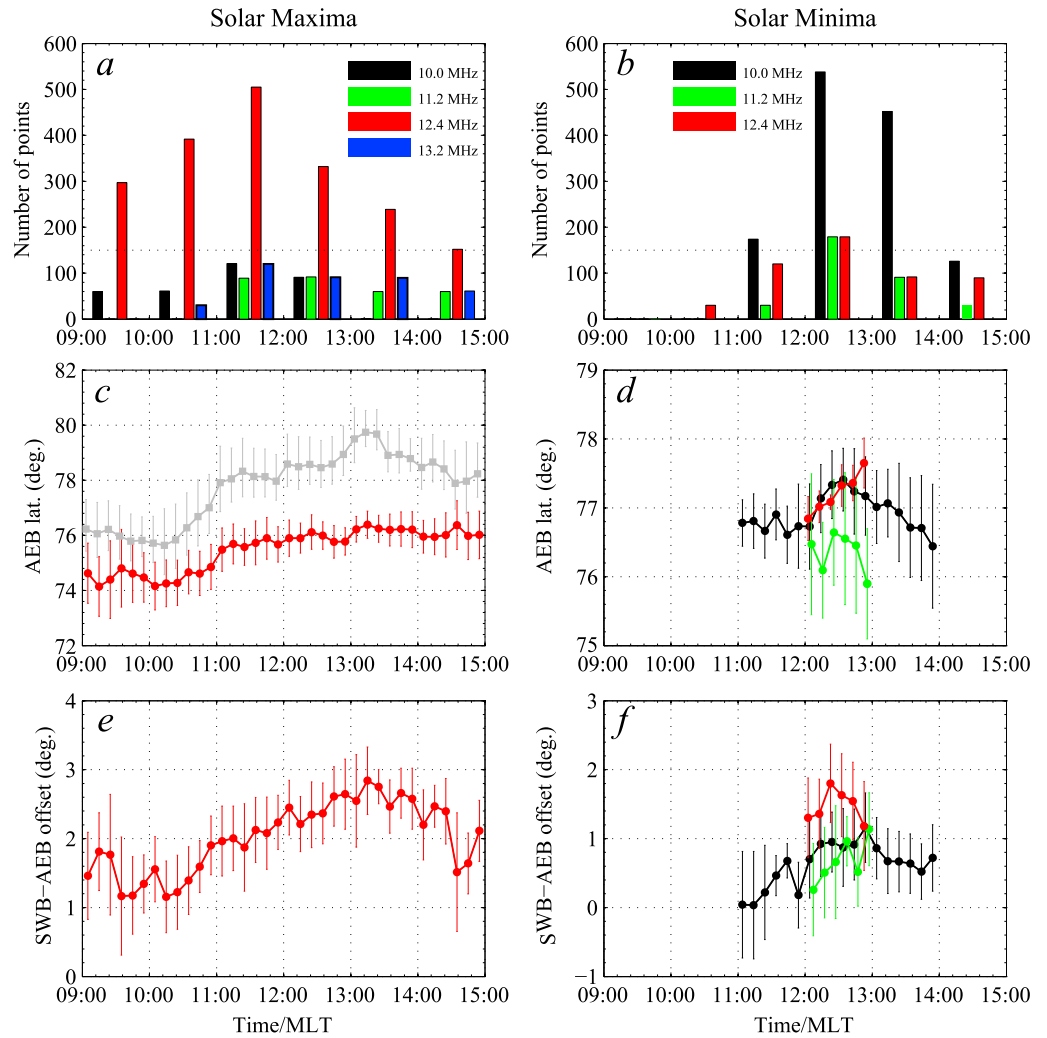


**Figure 4.** The distribution of data points versus MLT for different radar frequencies at solar (a) maxima and (b) minima. (c) The distribution of the AEB (red) and the SWB (grey) versus MLT for the radar frequency of 12.4 MHz. (d) The AEB versus MLT for radar frequencies of 10.0 MHz (black), 11.2 MHz (green), and 12.4 MHz (red) at solar minima. The corresponding SWB-AEB offset versus MLT at solar (e) maxima and (f) minima.

trend, which is consistent with observations of *Ruohoniemi and Greenwald [1997]* (see their plate 5 in winter) and *Lointier et al. [2008]* (see their Figure 1). The SWB-AEB offset in Figure 4e is smaller in the prenoon sector (~1.46° on average) than in the noon and postnoon sectors (~2.37°, peak at 13:15 MLT).

For solar minima in Figure 4d the distributions satisfying the selecting criteria are concentrated near noon, i.e., ~11:00–14:00 MLT. The mean AEB latitudes are located at ~76.91°, 76.35°, and 77.21° MLAT, respectively, for radar frequencies of 10.0 (black), 11.2 (green), and 12.4 (red) MHz. The concurrent SWB latitudes are not shown here to ensure clarity in the figure, but Figure 4f indicates that the mean SWB latitudes are located 0.62° (peak at 12:55 MLT), 0.67° (peak at 12:55 MLT), and 1.47° (peak at 12:25 MLT) poleward of the AEBs, respectively. Furthermore, the results in Figures 4e and 4f also show that the mean SWB-AEB offset in the postnoon sector (12:00–15:00 MLT) is generally larger than in the prenoon sector (09:00–12:00 MLT).

### 3.3. Range Variability

Although the peak SWB-AEB offset does not correspond to the highest AEB latitude, the increased SWB-AEB offset seems to be partly related to the poleward movement of the boundary, which has previously been observed by *Chisham et al. [2008]* and *Liu et al. [2012]*. They attributed this difference to the standard virtual

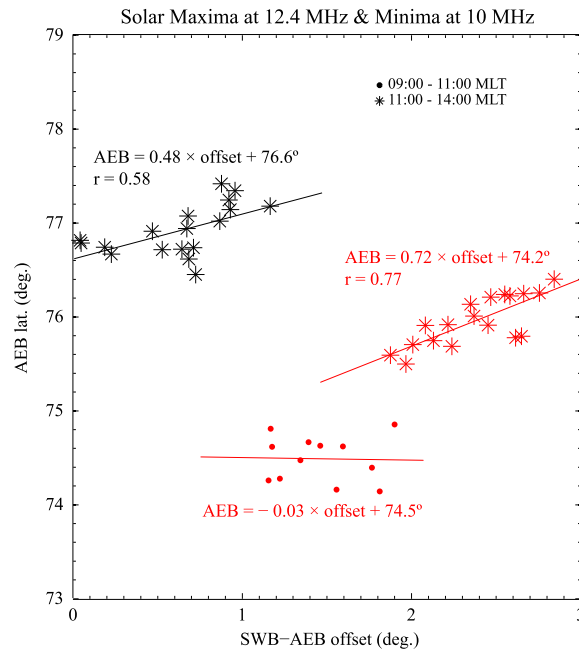


**Figure 5.** Scatterplots of SWB-AEB offset versus AEB latitude at solar maxima (red) and minima (black). The dots show observations before 11:00 MLT, while the stars represent observations after that.

height model used in the radar processing. In order to quantify the influence of the enhanced ionospheric density on the SWB-AEB offset, Figure 5 shows scatter plots of the mean SWB-AEB offset versus AEB latitude at solar maxima with radar frequency 12.4 MHz (red) and solar minima with radar frequency 10.0 MHz (black). The dots show observations before 11:00 MLT, while the stars show observation after that.

Looking at solar maxima, it can be seen that the observations before and after 11:00 MLT behave differently. Before 11:00 MLT there is only a small change in the auroral emission boundary with respect to changes in the SWB-AEB offset. After 11:00 MLT there is a large change in both the auroral emission boundary and the SWB-AEB offset with a slope coefficient for the fit equal to  $0.72 \pm 0.31$ . The increased SWB-AEB offset near noon is strongly related to the increasing ground range. However, for solar minima this trend is reduced to a slope coefficient of  $0.48 \pm 0.36$ . Considering the relationship between a raypath and the ground range [e.g., Chisham et al., 2008], the high coefficient is

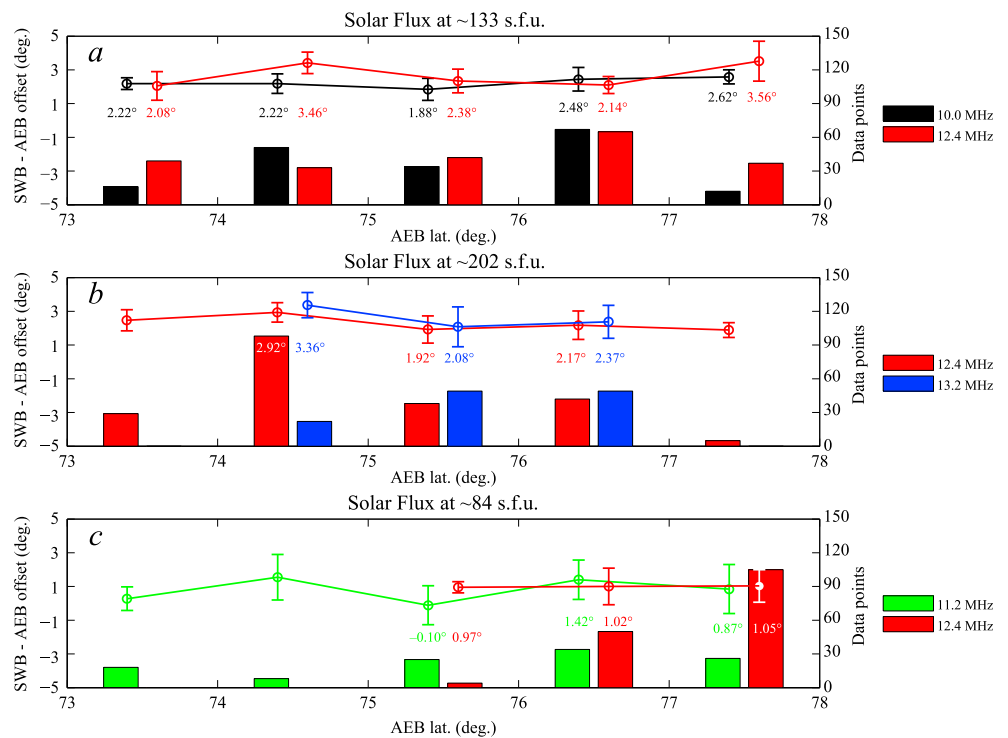


**Figure 6.** The distributions of median-filtered SWB-AEB offsets with latitude for different radar operating frequencies at (a-c) three different solar fluxes. The bar plots represent the distribution of data points, while colors illustrate the different radar operating frequencies.

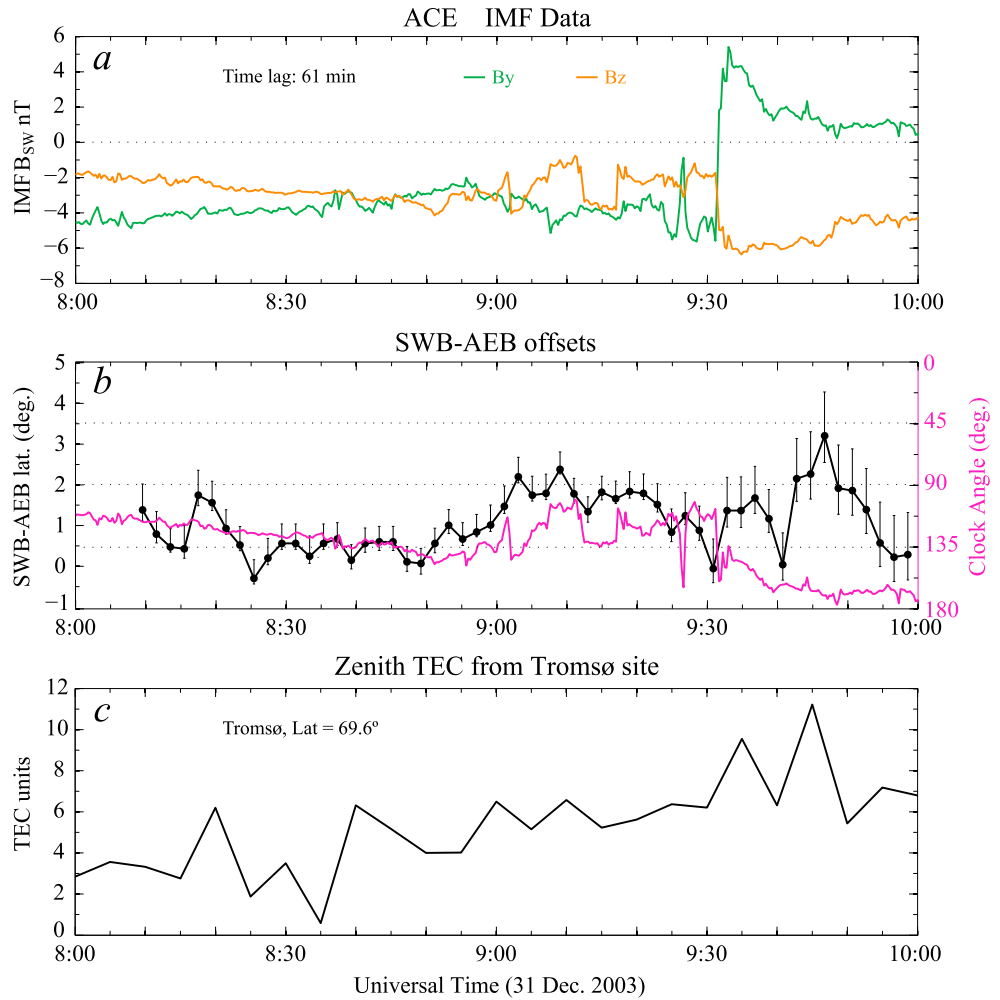


**Figure 7.** An example of simultaneous SWB-AEB offsets and ionospheric TEC from a GPS receiver at Tromsø. (a) The IMF  $B_y$  and  $B_z$  components from the ACE satellite. (b) The observed SWB-AEB offset versus time indicated by black dots. The error bars represent the probable mapping error from the assumed auroral emission height. The IMF clock angle is overlaid as a magenta curve. (c) The vertical TEC from Tromsø.

thought to be related to a large elevation angle of the raypath. As the ionospheric electron density is typically higher at solar maxima than minima [e.g., Cai *et al.*, 2008], the increased SWB-AEB offset strongly relies on the increasing ground range at solar maxima, which implies that the enhanced ionospheric density modulates the HF radar raypath more strongly.

### 3.4. Frequency Variability

However, the comparison of SWB-AEB offsets at solar maxima and minima in Figure 5 are for different radar frequencies. In order to investigate whether the varied radar frequencies have potential impact on the final mapping accuracy of the SWBs, Figure 6 compares the variation of median-filtered SWB-AEB offsets with ranges (i.e., different AEB latitudes) at the different radar operating frequencies. To reduce the probable influences of the changed solar flux and MLT, the contrast has been confined to similar solar  $F_{10.7}$  flux (i.e., 2002/2003 and 2013/2014 data used in Figure 6a, 2001/2002 used in Figure 6b, and 1998/1999 and 2004/2005 used in Figure 6c) and the same MLT (i.e., 12:00–13:00 MLT). The line plot with error bars represents the variation of the median-filtered SWB-AEB offset with the AEB latitudes, while the different colors represent the corresponding radar frequencies. The bar plot shows the distribution of data points within each latitude.

It can be easily seen that there is no distinct linear trend for the SWB-AEB offset along with the increased range. However, for nearly equal solar fluxes, i.e., for each panel, the SWB-AEB offsets with high radar frequencies are larger than for low radar frequencies at the same range, which means that the high radar frequency to a certain degree contributes to the final range accuracy.

### 3.5. A Case Study

The SWB-AEB offsets versus MLT peak near noon (see Figures 4e and 4f). Figure 7 presents an example of the SWB-AEB offset derived from Figure 2 and the simultaneous ionospheric total electron content (TEC) observations from a GPS receiver at a lower latitude (Tromsø) to illustrate the importance of the enhanced solar EUV high-density plasma in the postnoon sector (i.e., after ~09:00 UT). The interplanetary magnetic field (IMF)  $B_y$  and  $B_z$  component data from ACE, which was situated at (238, -25.5, 20.6)  $R_E$  in GSM coordinates, are shown in Figure 7a. With a solar wind speed of ~413 km/s, a ~61 min time lag from the satellite to the cusp ionosphere is estimated using the equation given by *Liou et al.* [1998] and *Lockwood et al.* [1989]. The southward IMF, with poleward moving auroral forms (see Figure 2a), is favorable for dayside low-latitude reconnection [*Sandholt et al.*, 1998]. IMF  $B_y$  is initially negative but abruptly changes to positive at 09:32 UT (~12:32 MLT), coincident with a sharp fall in IMF  $B_z$  to -6 nT.

The IMF clock angle, defined as  $\theta = \tan^{-1}(|B_y/B_z|)$  for  $B_z > 0$  and  $\theta = 180^\circ - \tan^{-1}(|B_y/B_z|)$  for  $B_z < 0$  in the GSM  $y$ - $z$  plane, is given by the magenta curve in Figure 7b. It varies between  $100^\circ$  and  $180^\circ$ . The SWB-AEB offset, with error bars representing the potential mapping errors from the assumed auroral altitude model, is overlaid in Figure 7b (black curve). The fluctuations are stronger in the postnoon sector, where the averaged SWB-AEB offset (~1.49°) increases twofold compared to the prenoon sector (~0.67°). The simultaneously estimated TEC values from the GPS receiver at the Tromsø site (see Figure 1, Glat.: 69.6°, Glon.: 19.2°; Finland radar beam 5 intersects it at range ~945 km) provide an estimate of TEC in 1 by 1° bins every 5 min [*Rideout and Coster*, 2006].

Figure 7c shows that the vertical ionospheric electron density increased from 3.75 TEC units in the prenoon sector to 6.74 TEC units in the postnoon sector. With the intake of high-density solar EUV ionized plasma from postnoon at subauroral latitudes [*Foster*, 1984; *Moen et al.*, 2006; *Lorentzen et al.*, 2010; *Oksavik et al.*, 2010; *Zhang et al.*, 2011, 2013b; *Chen et al.*, 2015], some peaks of the SWB-AEB offset partly associated with the enhanced IMF southward component are observed. This is particularly evident at 08:18, 09:04, 09:10, 09:36, and 09:46 UT where there is a clear correlation between the increased SWB-AEB offset and the enhanced TEC.

## 4. Discussion

Based on the simultaneous ground observations of OI 630.0 nm AEB and HF radar SWB along the geomagnetic meridian, covering winter season data from 1995/1996 to 2013/2014, a time-dependent statistical study of the SWB-AEB offset is performed. The ionospheric electron density is a crucial factor for SuperDARN HF radio wave propagation [e.g., *Milan et al.*, 1997; *Danskin et al.*, 2002; *Koustov et al.*, 2014], and the varied SWB-AEB offset should reflect the changed  $F$  region ionospheric electron density due to solar activity and ionospheric convection.

### 4.1. Validity of Results

The careful reader will notice that our SWB-AEB offset has some discrepancies compared to prior statistical results [e.g., *Chisham et al.*, 2005a; *Sotirelis et al.*, 2005; *Yeoman et al.*, 2008]. The SWBs measured by *Chisham et al.* [2005c] and the convection reversal boundaries derived by *Sotirelis et al.* [2005] were located 0–1° equatorward of the DMSP PPBs location near magnetic noon, which is smaller than the results presented here. However, by comparing with *Yeoman et al.*'s [2008] experiments that presented results from the same path (i.e., plasma irregularities generated by the SPEAR Heating facility in Longyearbyen on 17 April 2004), a difference in range accuracy (270 km in their Figure 4aiv) that is larger than our median-filtered SWB-AEB offset (1.57°, i.e., 170 km) in Figure 3 (2003/2004 winter season). These discrepancies could be due to different boundary finding algorithms and the database used. In our study, the acquired AEB is derived from a predefined reference model (see *Johnsen et al.* [2012] for more details), and an intimate relationship of the AEB with the PPB derived from the DMSP has been statistically confirmed by *Johnsen and Lorentzen* [2012a] (see their Figure 7b). For SuperDARN data, the robust boundaries from both *Chisham et al.* [2005c] and *Sotirelis et al.* [2005] were built at the cost of the temporal resolution of the boundary motion (10 min time resolution,

i.e., a median filter of adjacent beams and across five consecutive scans), while the range accuracy from Yeoman *et al.* [2008] was employed by the high backscatter power for each range gate. In our paper, the boundary finding algorithm adopts median filter to the adjacent range gate along geomagnetic meridian with 2 min time resolution (see Chen *et al.* [2015] for more details). On average the range accuracy should thus be larger than the results of Chisham *et al.* [2005c] and Sotirelis *et al.* [2005], but smaller than Yeoman *et al.* [2008]. In addition, we only used winter season data, the seasonal difference may also be one of the potential factors affecting the ionospheric plasma density and the range accuracy.

The improved SuperDARN virtual height model for mapping accuracy of ionospheric backscatter has also been derived and assessed by Chisham *et al.* [2008] and Yeoman *et al.* [2008], respectively. However, the standard virtual height model is still used in our study because the typical heights of natural and heater-induced ionospheric irregularities, as well as the path geometry for SuperDARN radars, are different. Although the AEB elevation angles have been confined, the assumed AEB height will inevitably introduce a mapping error at a certain degree. If the final mapping error of the ionospheric backscatter measured by the improved virtual height model is analogous to the AEB-introduced error, the reason for the SWB-AEB offset will be difficult to judge. Alternatively, a range correction algorithm using elevation angles has also been provided by Yeoman *et al.* [2008]. However, not all elevation angle data from Finland radar are calibrated and can be used in this study.

#### 4.2. Variation With Solar Cycle

The results presented here indicate quantitatively that the standard mapping technique utilized by the SuperDARN HF radars (i.e., that the HF radar path propagates to a fixed height along a straight line) produces some overestimation of the distances at far range [e.g., Chisham *et al.*, 2008; Yeoman *et al.*, 2008; Liu *et al.*, 2012]. Figure 3d shows that the SWB-AEB offset at solar maxima is approximately 2 times larger than at solar minima ( $\sim 2^\circ$  versus  $\sim 1^\circ$ ), even though the target irregularities (i.e., AEB) are typically located at a lower latitude (see Figure 3b). This indicates that the real raypath is strongly refracted at solar maxima. The  $F_{10.7}$  index characterizes the solar EUV irradiance [Tobiska *et al.*, 2000], which induces the vast majority of ionization in the sunlit ionosphere. The yearly variations of SWB-AEB offsets and solar flux, shown in Figures 3d and 3e with a Pearson correlation coefficient of 0.61, imply that the real radio wave propagation path is modulated by the varying background ionospheric conditions (see also Figure 7).

The dayside auroral zone is a hard target for coherent HF radars, and the propagation mode could be changed between  $1\frac{1}{2}$ -hop and  $\frac{1}{2}$ -hop randomly [Milan *et al.*, 1998]. However, the SuperDARN Finland radar is inclined to  $1\frac{1}{2}$ -hop propagation in the cusp region [e.g., Yeoman *et al.*, 2001, 2008; Danskin *et al.*, 2002]. Although the current data set did not consider possible changes in the propagation mode, the statistical result of Chisham *et al.* [2008] showed that the mapping error from the SuperDARN standard virtual height model (see their Figure 5, bottom panel), at  $\sim 1750$ – $2200$  km range (i.e., the majority of SWB latitudes at  $\sim 74^\circ$ – $78^\circ$  MLAT) was almost equal to the  $1\frac{1}{2}$ -hop and  $\frac{1}{2}$ -hop propagation modes. This means that the variable ionospheric density with solar activity is still a crucial reason for the mapping errors.

The electron density and peak height in the high-latitude  $F$  region is typically higher at solar maxima than minima [e.g., Cai *et al.*, 2008], to achieve that the maximum HF radio wave returns, the ionospheric refraction index must be stronger at solar maxima than minima [Gillies *et al.*, 2010], giving an increase in the returned ionospheric backscatter at higher elevation angles [Ponomarenko *et al.*, 2011]. This is also reflected in the observations that the rate of increase of SWB-AEB offset versus AEB latitude is higher at solar maxima than minima (see Figure 5 coefficients, 11:00–14:00 MLT). Statistical studies of the backscatter height and elevation angle at solar minima by Liu *et al.* [2012] (height:  $\sim 239$  km, angle:  $8^\circ$ – $10^\circ$  on average) and at solar maxima (but only at midnight) by Koustov *et al.* [2007] (height:  $\sim 275$  km, angle:  $\sim 12^\circ$  on average) illustrate that the enhanced solar activity influences the peak  $F$  region electron density. This in turn will influence the HF radio wave path and the location at which it achieves near orthogonality with the local geomagnetic field. This suggests that the mapping errors of the SWBs caused by the standard SuperDARN virtual height model [Chisham *et al.*, 2008; Liu *et al.*, 2012], which is modulated by the varied ionospheric condition due to the solar irradiance flux [Yeoman *et al.*, 2008; Chen *et al.*, 2015].

#### 4.3. Variation With MLT

The distributions of data points in Figures 4a and 4b show that the cusp is the most likely location for ionospheric HF radar echoes. The SWB-AEB offset becomes larger in the noon and postnoon sectors than the

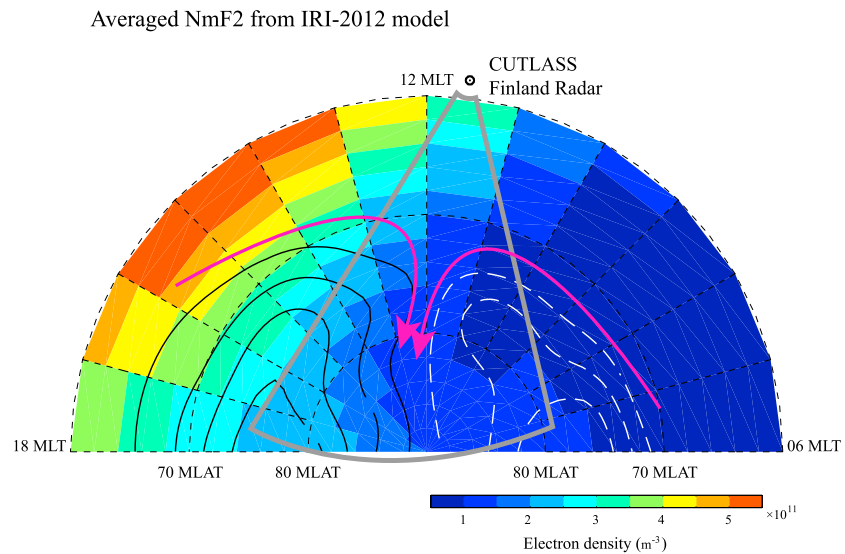


**Figure 8.** An illustration of the averaged  $N_m F_2$  distributions derived from the IRI-2012 model in December/January. The resolution of the color-coded grid cells is 1 h MLT and 2° geomagnetic latitude. Overlaid are the average convection pattern and the field of view of the SuperDARN Finland radar. See text for more details.

prenoon sector, while the peak SWB-AEB offsets (see Figures 4e and 4f) are all near noon. Due to the dayside reconnection electric field that controls the transport of EUV ionized plasma inflow from subauroral latitudes to cusp [e.g., Foster, 1984, 1993; Foster et al., 2005; Moen et al., 2006, 2008; Oksavik et al., 2010; Carlson et al., 2006; Zhang et al., 2013a, and references therein], the results imply that the low-density background plasma and high-density solar EUV ionized plasma could be redistributed at noon and postnoon sectors by ionospheric convection [Lockwood and Carlson, 1992; Pinnock et al., 1995; Moen et al., 2008], which would make the HF radar ray intersect more enhanced plasma in the cusp region.

A schematic explanation of the different  $F$  region density structures is shown in Figure 8. The color-coded grids represent yearly averaged distributions of  $F$  region ionospheric peak electron density ( $N_m F_2$ ) from the IRI-2012 model. The general dawn-dusk (white-black) convection cell derived from the SuperDARN convection model is overlaid. The fan-shaped grey line represents the field of view of the SuperDARN Finland radar at 09:00 UT, while the magenta arrows represent ionospheric convection through the cusp inflow region.

It can be easily seen that the high-density solar EUV ionized plasma is a persistent feature at subauroral latitude in the postnoon sector, while the dawnside ionospheric convection is mainly occupied by low-density plasma. The distribution of  $N_m F_2$  is consistent with the relatively large SWB-AEB offsets found in the noon and postnoon sectors, instead of the prenoon sector. However, the transport of high-density solar EUV ionized plasma through the cusp inflow region cannot distinctly reveal itself in IRI data, which have also been previously analyzed by Moen et al. [2008] that the chance of magnetopause reconnection and new intake of high-density solar EUV ionized plasma decreases for IMF  $B_z$  positive. This could explain why the observed linear variation of SWB-AEB offset with latitudes in Figure 5 is difficult to see in Figures 6 and 7. The linear fit in Figure 5 illustrates the role of the enhanced ionospheric density for HF radar raypath. As the solar EUV irradiance increases by as much as a factor of 3 over a solar cycle [e.g., Woods et al., 2005], it can be seen that the mean SWB-AEB offset at solar maxima is larger than at solar minima, even in the prenoon sector, which indicates that the increased SWB-AEB offset responds strongly to the enhanced ionospheric density.

However, the AEB is notably suppressed to low latitude in the prenoon hours (see Figure 4c). This is a little lower than the statistical AEB results at the same MLT by Johnsen and Lorentzen [2012b]. The reason is that not all observed auroral events can return the HF radar echoes because of the relatively low density and varied background ionospheric conditions. On the contrary, the decreased SWB-AEB offset in the postnoon sector (i.e., 14:00–15:00 MLT in Figure 4e) corresponds to the relatively stable AEB at high latitudes. The

geophysical factors that influence the discrepant variation of ionospheric density versus MLT should be taken into account [e.g., Ruohoniemi and Greenwald, 1997; Koustov *et al.*, 2014].

For the SuperDARN Finland radar the radio wave path is generally from low to high geomagnetic latitude, while the horizontal  $F$  region ionospheric density on the dayside is gradually decreasing with increasing latitude (see Figure 8). Nevertheless, the high-density solar EUV ionized plasma will only enter the cusp region from the postnoon sector due to convection [Foster, 1993]. The ionospheric plasma is mainly structured by low-density plasma from the prenoon sector, i.e., 09:00–11:00 MLT. But sometimes the enhanced plasma can initially be corotated past noon at lower latitudes, before being entrained in the afternoon convection pattern and brought back toward noon [Foster, 1993; Zhang *et al.*, 2013b]. This will enhance the  $F$  region plasma at low latitudes in the prenoon sector [e.g., Pinnock *et al.*, 1995], while the more poleward ionospheric density and the target location of the irregularities remains unchanged. The raypath will be strongly refracted by the lower latitude-enhanced  $F$  region density. However, in order to allow for a propagation path to the same location, a shorter raypath and smaller SWB-AEB offset will be needed [e.g., Yeoman *et al.*, 2008]. Nevertheless, the horizontal density gradient could be slightly different in the postnoon sector, compared to prenoon, because the prenoon to postnoon ratio of photoionization conductivity is  $\sim 0.33$  during the winter [Hu *et al.*, 2014]. The sharply enhanced ionospheric density, resulting from the intake of high-density solar EUV ionized plasma, will nearly cover the whole radio wave path in the noon sector, i.e., 11:00–14:00 MLT, which will produce a strong refraction, resulting in an increased overestimation of the SWB location.

#### 4.4. Variation With Radar Operation Frequency

When the ionospheric electron density encountered with the ray is constant, a change in radar frequency will result in a different refractive index for the radio wave at the same place [Ponomarenko *et al.*, 2009; Gillies *et al.*, 2011, 2012]. In order to quantify this effect, the median-filtered SWB-AEB offsets as a function of the frequencies at 12:00–13:00 MLT have been compared in Figure 6. Under nearly equal solar flux and range conditions, the median-filtered SWB-AEB offsets with high radar frequencies are mostly larger than with relatively low radar frequencies. This implies that the varied radar frequencies modulate the raypath, which could contribute to the varied SWB-AEB offset.

A multifrequency study of radio wave refraction effects was made by André *et al.* [1997] at solar maxima (February and September in 1988). They observed that the radio wave path (i.e., SWB-AEB offset) was shifted  $\sim 20$  km poleward when the radar frequency was changed from 11 to 12 MHz, and  $\sim 60$  km poleward for 11 to 14 MHz, which means that the refracted height of the radio wave path was elevated [Milan *et al.*, 2003a; Senior *et al.*, 2004]. However, the modeled analysis by a ray tracing program only showed 10 km poleward shifts when the radar frequency changed from 11 to 14 MHz, which was much lower than the experimental data. As there is no linear trend can be easily observed in Figure 6, through averaging the SWB-AEB offsets for different radar operating frequencies without taking account of the range differences, the SWB-AEB offsets will, on average, shift poleward by  $0.44^\circ$ ,  $0.2^\circ$ , and  $0.28^\circ$  latitude for radar frequencies varied from 10 to 12.4, 12.4 to 13.2, and 11.2 to 12.4 MHz, respectively. This means that the variable radar frequencies contribute to the range accuracy at an order of 20, 27, and 25 km with the solar flux at 133, 202, and 84 solar flux unit for a radar frequency change of 1 MHz, respectively. This is analogous to the result of André *et al.* [1997], which suggests that the varied radar frequencies affect the refraction of the radio wave differently for different  $F$  region ionospheric densities.

## 5. Conclusions

A statistical comparison of the difference in latitude between the HF radar SWB and the OI 630.0 nm AEB, versus solar activity, MLT, and radar operating frequency, has been carried out in this paper. Although some mapping errors inevitably come from the assumed auroral emission height, the optical mapping errors were significantly reduced by restricting the location of the 630.0 nm data to be near local zenith. The inherent SWB-AEB differences are therefore due to the virtual height model used by SuperDARN [Yeoman *et al.*, 2001, 2008; Chisham *et al.*, 2008], the results show that the  $F$  region density due to solar flux and MLT variations affects the refraction of the raypath and has a critical influence on the range accuracy of HF radar echoes.

A close relationship of median-filtered SWB-AEB offsets with solar cycle is demonstrated. The SWB-AEB offset at solar maxima is, on average, 2 times larger than at solar minima, while some offset discrepancies with prior

studies could be understood by considering the different boundary finding algorithms and database used. An asymmetric distribution of SWB-AEB offset versus MLT is associated with the ionospheric density at subauroral latitudes, which is modulated by transport of high-density solar EUV ionized plasma from the post-noon sector, which can only be visualized using severely smoothed values from the IRI model. An example of the simultaneous SWB-AEB offset and GPS TEC in Tromsø confirms this speculation. Due to the intake of high-density solar EUV ionized plasma from the postnoon sector to the cusp region, the peaks of SWB-AEB offset versus MLT tends to be located near noon. The mapped HF radar SWB will generally shift poleward in response to an enhanced  $F$  region density in the noon and postnoon sectors, while due to raypath geometry the different horizontal density gradient along the geomagnetic meridian would make the SWB-AEB offsets slightly different (i.e., unrelated to the ground range in the prenoon sector). The altered HF radar operating frequency also has a varied refraction effect that contributes to the final location of HF radar echoes. However, the detailed relationship of the SWB-AEB offset with the varied radar frequency versus a varying ionospheric density should be considered in future studies.

### Acknowledgments

This study has been supported by the Research Council of Norway under contracts 223252, 208006, and 230996. The CUTLASS Finland radar is part of SuperDARN and is supported by the RSPG group at the University of Leicester, the Swedish Institute of Space Physics, and the Finnish Meteorological Institute in Helsinki. The SuperDARN data can be retrieved from Virginia Tech. The Longyearbyen MSP is owned and operated by UNIS; the data can be obtained from Dag Lorentzen. The IRI-2012 model can be accessed through the website <http://iri.gsfc.nasa.gov/>. The monthly averaged  $F_{10.7}$  solar flux data were downloaded from Natural Resources Canada ([ftp://ftp.geolab.nrcan.gc.ca/data/solar\\_flux/](ftp://ftp.geolab.nrcan.gc.ca/data/solar_flux/)). We also thank the MIT Haystack Observatory for providing GPS TEC data which can be accessed through the website <http://madrigal.haystack.mit.edu/madrigal/>. The NASA CDAWeb site supplies the solar wind and IMF data from the ACE spacecraft (<http://cdaweb.gsfc.nasa.gov/>). M.L. acknowledges support from NERC via grant NE/K011766/1.

### References

- André, R., C. Hanuise, J. P. Villain, and J. C. Cerisier (1997), HF radars: Multifrequency study of refraction effects and localization of scattering, *Radio Sci.*, *32*(1), 153–168, doi:10.1029/96RS02987.
- Baker, K. B., and S. Wing (1989), A new magnetic coordinate system for conjugate studies at high latitudes, *J. Geophys. Res.*, *94*(A7), 9139, doi:10.1029/JA094iA07p09139.
- Baker, K. B., R. A. Greenwald, A. D. M. Walker, P. F. Bythrow, L. J. Zanetti, T. A. Potemra, D. A. Hardy, F. J. Rich, and C. L. Rino (1986), A case study of plasma processes in the dayside cleft, *J. Geophys. Res.*, *91*(A3), 3130, doi:10.1029/JA091iA03p3130.
- Baker, K. B., J. R. Dudeney, R. A. Greenwald, M. Pinnock, P. T. Newell, A. S. Rodger, N. Mattin, and C. I. Meng (1995), HF radar signatures of the cusp and low-latitude boundary layer, *J. Geophys. Res.*, *100*(A5), 7671, doi:10.1029/94JA01481.
- Billitz, D., D. Altdill, Y. Zhang, C. Mertens, V. Truhlik, P. Richards, L.-A. McKinnell, and B. Reinisch (2014), The International Reference Ionosphere 2012—A model of international collaboration, *J. Space Weather Space Clim.*, *4*, A07, doi:10.1051/swsc/2014004.
- Bjoland, L. M., X. Chen, Y. Jin, A. S. Reimer, Å. Skjæveland, M. R. Wessel, J. K. Burchill, L. B. N. Clausen, S. E. Haaland, and K. A. McWilliams (2015), Interplanetary magnetic field and solar cycle dependence of Northern Hemisphere  $F$  region joule heating, *J. Geophys. Res. Space Physics*, *120*, 1478–1487, doi:10.1002/2014JA020586.
- Cai, H. T., S. Y. Ma, Y. Fan, Y. C. Liu, and K. Schlegel (2008), Climatological features of electron density in the polar ionosphere from long-term observations of EISCAT/ESR radar, *Ann. Geophys.*, *25*(12), 2561–2569, doi:10.5194/angeo-25-2561-2007.
- Carlson, H. C., K. Oksavik, J. Moen, and T. Pedersen (2004), Ionospheric patch formation: Direct measurements of the origin of a polar cap patch, *Geophys. Res. Lett.*, *31*, L08806, doi:10.1029/2003GL018166.
- Carlson, H. C., J. Moen, K. Oksavik, C. P. Nielsen, I. W. McCrea, T. R. Pedersen, and P. Gallop (2006), Direct observations of injection events of subauroral plasma into the polar cap, *Geophys. Res. Lett.*, *33*, L05103, doi:10.1029/2005GL025230.
- Chen, X. C., D. A. Lorentzen, J. I. Moen, K. Oksavik, and L. J. Baddeley (2015), Simultaneous ground-based optical and HF radar observations of the ionospheric footprint of the open/closed field line boundary along the geomagnetic meridian, *J. Geophys. Res. Space Physics*, *120*, 9859–9874, doi:10.1002/2015JA021481.
- Chisham, G., and M. P. Freeman (2003), A technique for accurately determining the cusp-region polar cap boundary using SuperDARN HF radar measurements, *Ann. Geophys.*, *21*(4), 983–996, doi:10.5194/angeo-21-983-2003.
- Chisham, G., and M. P. Freeman (2004), An investigation of latitudinal transitions in the SuperDARN Doppler spectral width parameter at different magnetic local times, *Ann. Geophys.*, *22*(4), 1187–1202, doi:10.5194/angeo-22-1187-2004.
- Chisham, G., M. P. Freeman, M. M. Lam, G. A. Abel, T. Sotirelis, R. A. Greenwald, and M. Lester (2005a), A statistical comparison of SuperDARN spectral width boundaries and DMSP particle precipitation boundaries in the afternoon sector ionosphere, *Ann. Geophys.*, *23*(12), 3645–3654, doi:10.5194/angeo-23-3645-2005.
- Chisham, G., M. P. Freeman, T. Sotirelis, and R. A. Greenwald (2005b), The accuracy of using the spectral width boundary measured in off-meridional SuperDARN HF radar beams as a proxy for the open-closed field line boundary, *Ann. Geophys.*, *23*(7), 2599–2604, doi:10.5194/angeo-23-2599-2005.
- Chisham, G., M. P. Freeman, T. Sotirelis, R. A. Greenwald, M. Lester, and J. P. Villain (2005c), A statistical comparison of SuperDARN spectral width boundaries and DMSP particle precipitation boundaries in the morning sector ionosphere, *Ann. Geophys.*, *23*(3), 733–743, doi:10.5194/angeo-23-733-2005.
- Chisham, G., et al. (2007), A decade of the Super Dual Auroral Radar Network (SuperDARN): Scientific achievements, new techniques and future directions, *Surv. Geophys.*, *28*(1), 33–109, doi:10.1007/s10712-007-9017-8.
- Chisham, G., T. K. Yeoman, and G. J. Sofko (2008), Mapping ionospheric backscatter measured by the SuperDARN HF radars—Part 1: A new empirical virtual height model, *Ann. Geophys.*, *26*(4), 823–841, doi:10.5194/angeo-26-823-2008.
- Cousins, E., and S. Shepherd (2010), A dynamical model of high-latitude convection derived from SuperDARN plasma drift measurements, *J. Geophys. Res.*, *115*, A12329, doi:10.1029/2010JA016017.
- Cowley, S. (2000), Magnetosphere-ionosphere interactions: A tutorial review, *Magnetospheric Current Systems*, *Geophys. Monogr. Ser.*, *118*, 91–106.
- Danskin, D. W., A. V. Koustov, T. Ogawa, N. Nishitani, S. Nozawa, S. E. Milan, M. Lester, and D. Andre (2002), On the factors controlling occurrence of  $F$  region coherent echoes, *Ann. Geophys.*, *20*(9), 1385–1397, doi:10.5194/angeo-20-1385-2002.
- Foster, J. C. (1984), Ionospheric signatures of magnetospheric convection, *J. Geophys. Res.*, *89*(A2), 855–865, doi:10.1029/JA089iA02p00855.
- Foster, J. C. (1993), Storm time plasma transport at middle and high latitudes, *J. Geophys. Res.*, *98*(A2), 1675–1689, doi:10.1029/92JA02032.
- Foster, J. C., A. J. Coster, P. J. Erickson, F. J. Rich, and B. R. Sandel (2004), Stormtime observations of the flux of plasmaspheric ions to the dayside cusp/magnetopause, *Geophys. Res. Lett.*, *31*, L08809, doi:10.1029/2004GL020082.
- Foster, J. C., et al. (2005), Multiradar observations of the polar tongue of ionization, *J. Geophys. Res.*, *110*, A09531, doi:10.1029/2004JA010928.

- Freeman, M. P., and G. Chisham (2004), On the probability distributions of SuperDARN Doppler spectral width measurements inside and outside the cusp, *Geophys. Res. Lett.*, *31*, L22802, doi:10.1029/2004GL020923.
- Gillies, R. G., G. C. Hussey, G. J. Sofko, D. M. Wright, and J. A. Davies (2010), A comparison of EISCAT and SuperDARN *F* region measurements with consideration of the refractive index in the scattering volume, *J. Geophys. Res.*, *115*, A06319, doi:10.1029/2009JA014694.
- Gillies, R. G., G. C. Hussey, G. J. Sofko, P. V. Ponomarenko, and K. A. McWilliams (2011), Improvement of HF coherent radar line-of-sight velocities by estimating the refractive index in the scattering volume using radar frequency shifting, *J. Geophys. Res.*, *116*, A01302, doi:10.1029/2010JA016043.
- Gillies, R. G., G. C. Hussey, G. J. Sofko, and K. A. McWilliams (2012), A statistical analysis of SuperDARN scattering volume electron densities and velocity corrections using a radar frequency shifting technique, *J. Geophys. Res.*, *117*, A08320, doi:10.1029/2012JA017866.
- Greenwald, R. A., K. B. Baker, R. A. Hutchins, and C. Hanuise (1985), An HF phased-array radar for studying small-scale structure in the high-latitude ionosphere, *Radio Sci.*, *20*(1), 63–79, doi:10.1029/RS020i001p00063.
- Greenwald, R. A., et al. (1995), DARN/SuperDARN A global view of the dynamics of high-latitude convection, *Space Sci. Rev.*, *71*(1–4), 761–796, doi:10.1007/BF00751350.
- Greenwald, R. A., K. Oksavik, R. Barnes, J. M. Ruohoniemi, J. Baker, and E. R. Talaat (2008), First radar measurements of ionospheric electric fields at sub-second temporal resolution, *Geophys. Res. Lett.*, *35*, L03111, doi:10.1029/2007GL032164.
- Hu, Z.-J., Y. Ebihara, H.-G. Yang, H.-Q. Hu, B.-C. Zhang, B. Ni, R. Shi, and T. S. Trondsen (2014), Hemispheric asymmetry of the structure of dayside auroral oval, *Geophys. Res. Lett.*, *41*, 8696–8703, doi:10.1002/2014GL062345.
- Johnsen, M. G., and D. A. Lorentzen (2012a), The dayside open/closed field line boundary as seen from space- and ground-based instrumentation, *J. Geophys. Res.*, *117*, A03320, doi:10.1029/2011JA016983.
- Johnsen, M. G., and D. A. Lorentzen (2012b), A statistical analysis of the optical dayside open/closed field line boundary, *J. Geophys. Res.*, *117*, A02218, doi:10.1029/2011JA016984.
- Johnsen, M. G., D. A. Lorentzen, J. M. Holmes, and U. P. Løvhaug (2012), A model based method for obtaining the open/closed field line boundary from the cusp auroral 6300 Å[OI] red line, *J. Geophys. Res.*, *117*, A03319, doi:10.1029/2011JA016980.
- Knudsen, W. (1974), Magnetospheric convection and the high-latitude  $F_2$  ionosphere, *J. Geophys. Res.*, *79*(7), 1046–1055, doi:10.1029/JA079i007p01046.
- Koustov, A., D. André, E. Turunen, T. Raito, and S. Milan (2007), Heights of SuperDARN *F* region echoes estimated from the analysis of HF radio wave propagation, *Ann. Geophys.*, *25*(9), 1987–1994, doi:10.5194/angeo-25-1987-2007.
- Koustov, A. V., P. V. Ponomarenko, M. Ghezelbash, D. R. Themens, and P. T. Jayachandran (2014), Electron density and electric field over Resolute Bay and *F* region ionospheric echo detection with the Rankin Inlet and Inuvik SuperDARN radars, *Radio Sci.*, *49*, 1194–1205, doi:10.1002/2014RS005579.
- Lester, M., P. J. Chapman, S. W. H. Cowley, S. J. Crooks, J. A. Davies, P. Hamadyk, K. A. McWilliams, S. E. Milan, M. J. Parsons, and D. B. Payne (2004), Stereo CUTLASS—A new capability for the SuperDARN HF radars, *Ann. Geophys.*, *22*(2), 459–473, doi:10.5194/angeo-22-459-2004.
- Liou, K., P. T. Newell, C. I. Meng, M. Brittnacher, and G. Parks (1998), Characteristics of the solar wind controlled auroral emissions, *J. Geophys. Res.*, *103*(A8), 17,543, doi:10.1029/98JA01388.
- Liu, E. X., H. Q. Hu, R. Y. Liu, Z. S. Wu, and M. Lester (2012), An adjusted location model for SuperDARN backscatter echoes, *Ann. Geophys.*, *30*(12), 1769–1779, doi:10.5194/angeo-30-1769-2012.
- Lockwood, M., and H. C. Carlson (1992), Production of polar cap electron density patches by transient magnetopause reconnection, *Geophys. Res. Lett.*, *19*(17), 1731–1734, doi:10.1029/92GL01993.
- Lockwood, M., P. E. Sandholt, S. W. H. Cowley, and T. Oguti (1989), Interplanetary magnetic field control of dayside auroral activity and the transfer of momentum across the dayside magnetopause, *Planet. Space Sci.*, *37*(11), doi:10.1016/0032-0633(89)90106-2.
- Lockwood, M., S. W. H. Cowley, and M. P. Freeman (1990), The excitation of plasma convection in the high-latitude ionosphere, *J. Geophys. Res.*, *95*(A6), 7961, doi:10.1029/JA095iA06p07961.
- Lointier, G., T. Dudok de Wit, C. Hanuise, X. Vallières, and J.-P. Villain (2008), A statistical approach for identifying the ionospheric footprint of magnetospheric disturbances from SuperDARN observations, *Ann. Geophys.*, *26*(2), 305–314, doi:10.5194/angeo-26-305-2008.
- Lorentzen, D. A., C. S. Deehr, J. I. Minow, R. W. Smith, H. C. Stenbaek-Neilsen, F. Sigernes, R. L. Arnoldy, and K. Lynch (1996), SCIFER-Dayside auroral signatures of magnetospheric energetic electrons, *Geophys. Res. Lett.*, *23*(14), 1885–1888, doi:10.1029/96GL00593.
- Lorentzen, D. A., J. Moen, K. Oksavik, F. Sigernes, Y. Saito, and M. G. Johnsen (2010), In situ measurement of a newly created polar cap patch, *J. Geophys. Res.*, *115*, A12323, doi:10.1029/2010JA015710.
- Milan, S. E., T. K. Yeoman, M. Lester, E. C. Thomas, and T. B. Jones (1997), Initial backscatter occurrence statistics from the CUTLASS HF radars, *Ann. Geophys.*, *15*(6), 703–718, doi:10.1007/s00585-997-0703-0.
- Milan, S. E., T. K. Yeoman, and M. Lester (1998), The dayside auroral zone as a hard target for coherent HF radars, *Geophys. Res. Lett.*, *25*(19), 3717–3720, doi:10.1029/98GL02781.
- Milan, S. E., M. Lester, S. W. H. Cowley, J. Moen, P. E. Sandholt, and C. J. Owen (1999), Meridian-scanning photometer, coherent HF radar, and magnetometer observations of the cusp: A case study, *Ann. Geophys.*, *17*(2), 159–172, doi:10.1007/s00585-999-0159-5.
- Milan, S. E., M. Lester, and N. Sato (2003a), Multi-frequency observations of *E* region HF radar aurora, *Ann. Geophys.*, *21*(3), 761–777.
- Milan, S. E., M. Lester, S. Cowley, K. Oksavik, M. Brittnacher, R. Greenwald, G. Sofko, and J.-P. Villain (2003b), Variations in the polar cap area during two substorm cycles, *Ann. Geophys.*, *21*(5), 1121–1140, doi:10.5194/angeo-21-1121-2003.
- Milan, S. E., J. S. Gosling, and B. Hubert (2012), Relationship between interplanetary parameters and the magnetopause reconnection rate quantified from observations of the expanding polar cap, *J. Geophys. Res.*, *117*, A03226, doi:10.1029/2011JA017082.
- Moen, J., M. Lockwood, P. Sandholt, U. Løvhaug, W. Denig, A. Van Eyken, and A. Egeland (1996), Variability of dayside high latitude convection associated with a sequence of auroral transients, *J. Atmos. Terr. Phys.*, *58*(1), 85–96, doi:10.1016/0021-9169(95)00021-6.
- Moen, J., D. A. Lorentzen, and F. Sigernes (1998), Dayside moving auroral forms and bursty proton auroral events in relation to particle boundaries observed by NOAA 12, *J. Geophys. Res.*, *103*(A7), 14855, doi:10.1029/97JA02877.
- Moen, J., H. C. Carlson, S. E. Milan, N. Shumilov, B. Lybekk, P. E. Sandholt, and M. Lester (2001), On the collocation between dayside auroral activity and coherent HF radar backscatter, *Ann. Geophys.*, *18*(12), 1531–1549, doi:10.1007/s00585-001-1531-2.
- Moen, J., I. K. Walker, L. Kersley, and S. E. Milan (2002), On the generation of cusp HF backscatter irregularities, *J. Geophys. Res.*, *107*(A4), doi:10.1029/2001JA000111.
- Moen, J., M. Lockwood, K. Oksavik, H. Carlson, W. Denig, A. Van Eyken, and I. McCrea (2004), The dynamics and relationships of precipitation, temperature and convection boundaries in the dayside auroral ionosphere, *Ann. Geophys.*, *22*(6), 1973–1987, doi:10.5194/angeo-22-1973-2004.

- Moen, J., H. C. Carlson, K. Oksavik, C. P. Nielsen, S. E. Pryse, H. R. Middleton, I. W. McCreia, and P. Gallop (2006), EISCAT observations of plasma patches at sub-auroral cusp latitudes, *Ann. Geophys.*, *24*(9), 2363–2374, doi:10.5194/angeo-24-2363-2006.
- Moen, J., X. C. Qiu, H. C. Carlson, R. Fujii, and I. W. McCreia (2008), On the diurnal variability in  $F_2$  region plasma density above the EISCAT Svalbard radar, *Ann. Geophys.*, *26*(8), 2427–2433, doi:10.5194/angeo-26-2427-2008.
- Moen, J., K. Oksavik, T. Abe, M. Lester, Y. Saito, T. A. Bekkeng, and K. S. Jacobsen (2012), First in-situ measurements of HF radar echoing targets, *Geophys. Res. Lett.*, *39*, L07104, doi:10.1029/2012GL051407.
- Moen, J., K. Oksavik, L. Alfonsi, Y. Daabakk, V. Romano, and L. Spogli (2013), Space weather challenges of the polar cap ionosphere, *J. Space Weather Space Clim.*, *3*, A02, doi:10.1051/swsc/2013025.
- Newell, P. T., and C. I. Meng (1992), Mapping the dayside ionosphere to the magnetosphere according to particle precipitation characteristics, *Geophys. Res. Lett.*, *19*(6), 609–612, doi:10.1029/92GL00404.
- Nishimura, Y., et al. (2014), Day-night coupling by a localized flow channel visualized by polar cap patch propagation, *Geophys. Res. Lett.*, *41*, 3701–3709, doi:10.1002/2014GL060301.
- Oksavik, K., F. Søråas, J. Moen, and W. J. Burke (2000), Optical and particle signatures of magnetospheric boundary layers near magnetic noon: Satellite and ground-based observations, *J. Geophys. Res.*, *105*(A12), 27,555–27,568, doi:10.1029/1999JA000237.
- Oksavik, K., J. Moen, and H. C. Carlson (2004a), High-resolution observations of the small-scale flow pattern associated with a poleward moving auroral form in the cusp, *Geophys. Res. Lett.*, *31*, L11807, doi:10.1029/2004GL019838.
- Oksavik, K., F. Søråas, J. Moen, R. Pfaff, J. A. Davies, and M. Lester (2004b), Simultaneous optical, CUTLASS HF radar, and FAST spacecraft observations: Signatures of boundary layer processes in the cusp, *Ann. Geophys.*, *22*(2), 511–525, doi:10.5194/angeo-22-511-2004.
- Oksavik, K., J. M. Ruohoniemi, R. A. Greenwald, J. B. H. Baker, J. Moen, H. C. Carlson, T. K. Yeoman, and M. Lester (2006), Observations of isolated polar cap patches by the European Incoherent Scatter (EISCAT) Svalbard and Super Dual Auroral Radar Network (SuperDARN) Finland radars, *J. Geophys. Res.*, *111*, A05310, doi:10.1029/2005JA011400.
- Oksavik, K., V. L. Barth, J. Moen, and M. Lester (2010), On the entry and transit of high-density plasma across the polar cap, *J. Geophys. Res.*, *115*, A12308, doi:10.1029/2010JA015817.
- Oksavik, K., J. I. Moen, E. H. Rekaa, H. C. Carlson, and M. Lester (2011), Reversed flow events in the cusp ionosphere detected by SuperDARN HF radars, *J. Geophys. Res.*, *116*, A12303, doi:10.1029/2011JA016788.
- Oksavik, K., J. Moen, M. Lester, T. A. Bekkeng, and J. K. Bekkeng (2012), In situ measurements of plasma irregularity growth in the cusp ionosphere, *J. Geophys. Res.*, *117*, A11301, doi:10.1029/2012JA017835.
- Pinnock, M., A. Rodger, and F. Berkey (1995), High-latitude F region electron concentration measurements near noon: A case study, *J. Geophys. Res.*, *100*(A5), 7723–7729, doi:10.1029/94JA02558.
- Ponomarenko, P. V., and C. L. Waters (2006), Spectral width of SuperDARN echoes: Measurement, use and physical interpretation, *Ann. Geophys.*, *24*(1), 115–128, doi:10.5194/angeo-24-115-2006.
- Ponomarenko, P. V., C. L. Waters, and F. W. Menk (2007), Factors determining spectral width of HF echoes from high latitudes, *Ann. Geophys.*, *25*, 675–687, doi:10.5194/angeo-25-675-2007.
- Ponomarenko, P. V., J.-P. St-Maurice, C. L. Waters, R. G. Gillies, and A. V. Koustov (2009), Refractive index effects on the scatter volume location and Doppler velocity estimates of ionospheric HF backscatter echoes, *Ann. Geophys.*, *27*(11), 4207–4219, doi:10.5194/angeo-27-4207-2009.
- Ponomarenko, P. V., A. V. Koustov, J. P. St-Maurice, and J. Wiid (2011), Monitoring the F region peak electron density using HF backscatter interferometry, *Geophys. Res. Lett.*, *38*, L21102, doi:10.1029/2011GL049675.
- Rideout, W., and A. Coster (2006), Automated GPS processing for global total electron content data, *GPS Solut.*, *10*(3), 219–228, doi:10.1007/s10291-006-0029-5.
- Rodger, A. S., S. B. Mende, T. J. Rosenberg, and K. B. Baker (1995), Simultaneous optical and HF radar observations of the ionospheric cusp, *Geophys. Res. Lett.*, *22*(15), 2045–2048, doi:10.1029/95GL01797.
- Romick, G. J. (1976), The detection and study of the visible spectrum of the aurora and airglow, in *Methods for Atmospheric Radiometry*, August 26–27, 1976, San Diego, California, edited by D. P. McNutt, pp. 63–70, Soc. of Photo-optical Instrum. Eng., Palos Verdes Estates, Calif.
- Ruohoniemi, J. M., and R. A. Greenwald (1997), Rates of scattering occurrence in routine HF radar observations during solar cycle maximum, *Radio Sci.*, *32*(3), 1051–1070, doi:10.1029/97rs00116.
- Sandholt, P. E., C. J. Farrugia, J. Moen, Ø. Noraberg, B. Lybakk, T. Sten, and T. Hansen (1998), A classification of dayside auroral forms and activities as a function of interplanetary magnetic field orientation, *J. Geophys. Res.*, *103*(A10), 23,325, doi:10.1029/98JA02156.
- Senior, A., N. Borisov, M. Kosch, T. Yeoman, F. Honary, and M. Rietveld (2004), Multi-frequency HF radar measurements of artificial F region field-aligned irregularities, *Ann. Geophys.*, *22*, 3503–3512, doi:10.5194/angeo-22-3503-2004.
- Sojka, J. J., M. Bowline, and R. W. Schunk (1994), Patches in the polar ionosphere: UT and seasonal dependence, *J. Geophys. Res.*, *99*(A8), 14,959–14,970, doi:10.1029/93JA03327.
- Sotirelis, T., J. M. Ruohoniemi, R. J. Barnes, P. T. Newell, R. A. Greenwald, J. P. Skura, and C. I. Meng (2005), Comparison of SuperDARN radar boundaries with DMSP particle precipitation boundaries, *J. Geophys. Res.*, *110*, A06302, doi:10.1029/2004JA010732.
- Tobiska, W. K., T. Woods, F. Eparvier, R. Viereck, L. Floyd, D. Bouwer, G. Rottman, and O. White (2000), The SOLAR2000 empirical solar irradiance model and forecast tool, *J. Atmos. Sol. Terr. Phys.*, *62*(14), 1233–1250, doi:10.1016/S1364-6826(00)00070-5.
- Vallières, X., J. P. Villain, and R. André (2003), Characterization of frequency effect in SuperDARN spectral width distributions, *Radio Sci.*, *38*(1), 1003, doi:10.1029/2001RS002550.
- Villain, J. P., R. A. Greenwald, and J. F. Vickrey (1984), HF ray tracing at high latitudes using measured meridional electron density distributions, *Radio Sci.*, *19*(1), 359–374, doi:10.1029/RS019i001p00359.
- Woods, T. N., F. G. Eparvier, S. M. Bailey, P. C. Chamberlin, J. Lean, G. J. Rottman, S. C. Solomon, W. K. Tobiska, and D. L. Woodraska (2005), Solar EUV Experiment (SEE): Mission overview and first results, *J. Geophys. Res.*, *110*, A01312, doi:10.1029/2004JA010765.
- Yeoman, T. K., D. M. Wright, A. J. Stocker, and T. B. Jones (2001), An evaluation of range accuracy in the Super Dual Auroral Radar Network over-the-horizon HF radar systems, *Radio Sci.*, *36*(4), 801–813, doi:10.1029/2000RS002558.
- Yeoman, T. K., G. Chisham, L. J. Baddeley, R. S. Dhillon, T. J. T. Karhunen, A. Senior, and D. M. Wright (2008), Mapping ionospheric backscatter measured by the SuperDARN HF radars—Part 2: Assessing SuperDARN virtual height models, *Ann. Geophys.*, *26*(4), 843–852, doi:10.5194/angeo-26-843-2008.
- Zhang, Q. H., et al. (2011), On the importance of interplanetary magnetic field  $|B_y|$  on polar cap patch formation, *J. Geophys. Res.*, *116*, A05308, doi:10.1029/2010JA016287.
- Zhang, Q. H., et al. (2013a), Direct observations of the evolution of polar cap ionization patches, *Science*, *339*(6127), 1597–1600, doi:10.1126/science.1231487.

- Zhang, Q. H., B. C. Zhang, J. Moen, M. Lockwood, I. W. McCrea, H. G. Yang, H. Q. Hu, R. Y. Liu, S. R. Zhang, and M. Lester (2013b), Polar cap patch segmentation of the tongue of ionization in the morning convection cell, *Geophys. Res. Lett.*, *40*, 2918–2922, doi:10.1002/grl.50616.
- Zhang, Q. H., M. Lockwood, J. Foster, S. R. Zhang, B. C. Zhang, I. McCrea, J. Moen, M. Lester, and J. M. Ruohoniemi (2015), Direct observations of the full Dungey convection cycle in the polar ionosphere for southward interplanetary magnetic field conditions, *J. Geophys. Res. Space Physics*, *120*, 4519–4530, doi:10.1002/2015JA021172.